Chemical
Science

EDGE ARTICLE

View Article Online
View Journal | View Issue

Check for updates

Cite this: *Chem. Sci.*, 2022, **13**, 13489

All publication charges for this article have been paid for by the Royal Society of Chemistry

Cardiolipin, and not monolysocardiolipin, preferentially binds to the interface of complexes III and IV†

Robin A. Corey, ‡[a] Noah Harrison,‡§[a] Philllp J. Stansfeld,[b] Mark S. P. Sansom [a] and Anna L. Duncan ¶*[a]

Received 21st July 2022
Accepted 25th October 2022

DOI: 10.1039/d2sc04072g

rsc.li/chemical-science

The mitochondrial electron transport chain comprises a series of protein complexes embedded in the inner mitochondrial membrane that generate a proton motive force *via* oxidative phosphorylation, ultimately generating ATP. These protein complexes can oligomerize to form larger structures called supercomplexes. Cardiolipin (CL), a conical lipid, unique within eukaryotes to the inner mitochondrial membrane, has proven essential in maintaining the stability and function of supercomplexes. Monolysocardiolipin (MLCL) is a CL variant that accumulates in people with Barth syndrome (BTHS). BTHS is caused by defects in CL biosynthesis and characterised by abnormal mitochondrial bioenergetics and destabilised supercomplexes. However, the mechanisms by which MLCL causes pathogenesis remain unclear. Here, multiscale molecular dynamics characterise the interactions of CL and MLCL with yeast and mammalian mitochondrial supercomplexes containing complex III (CIII) and complex IV (CIV). Coarse-grained simulations reveal that both CL and MLCL bind to sites at the interface between CIII and CIV of the supercomplex. Free energy perturbation calculations show that MLCL interaction is weaker than that of CL and suggest that interaction with CIV drives this difference. Atomistic contact analyses show that, although interaction with CIII is similar for CL and MLCL, CIV makes more contacts with CL than MLCL, demonstrating that CL is a more successful "glue" between the two complexes. Simulations of the human $CIII_2CIV$ supercomplex show that this interface site is maintained between species. Our study suggests that MLCL accumulation in people with BTHS disrupts supercomplex stability by formation of relatively weak interactions at the interface lipid binding site.

Introduction

The mitochondrial electron transport chain is responsible for the generation of ATP at the mitochondrial inner membrane. It includes the respiratory complexes cytochrome bc_1 (or complex III, CIII) and cytochrome *c* oxidase (or complex IV, CIV). CIII catalyses the oxidation of the lipid soluble co-factor ubiquinol and simultaneously reduces the mobile electron transporter cytochrome *c* (cyt *c*). CIV transfers electrons from cyt *c* to oxygen to form water.[1] Both complexes can co-assemble into larger supercomplex structures, although the composition and stoichiometry varies.[2] While the functional significance of supercomplexes remains unsettled, many hypotheses have been proposed. It has been suggested that formation of supercomplexes may increase the stability of individual respiratory complexes; reduce production of harmful reactive oxygen species; or increase electron transfer efficiency between complexes.[2] Recently, it has been proposed that the association of CIII and CIV into a supercomplex structure reduces the distance that the mobile electron carrier, cyt *c*, has to travel between the two.[3,4] Another explanation for supercomplex existence postulates that the structures allow for the unusually high concentration of proteins seen in the inner mitochondrial membrane (IMM). Supercomplex formation is therefore thought to reduce the energetic costs of protein crowding and prevent unproductive protein aggregation.[5,6]

Cardiolipin (CL) constitutes up to 20% of the IMM phospholipid content[7] and exhibits unique molecular properties as a result of its conical shape, with a small headgroup consisting of two phosphate groups linked by a glycerol bridge, bound to four acyl chains. Direct protein-CL interactions have been shown to influence both protein stability and activity in a range

---

[a] *Department of Biochemistry, University of Oxford, South Parks Road, Oxford, OX1 3QU, UK. E-mail: anna.duncan@chem.au.dk*

[b] *School of Life Sciences & Department of Chemistry, University of Warwick, Coventry, CV4 7AL, UK*

† Electronic supplementary information (ESI) available: lipid interaction sites and CL to MLCL parameters used for free energy perturbation. See DOI: https://doi.org/10.1039/d2sc04072g

‡ Contributed equally.

§ Current address: Evariste, Southdene Thames Road, Goring, Reading, RG8 9AL, UK.

¶ Current address: Department of Chemistry, Aarhus University, Lagelandsgade 140, 8000 Aarhus C, Denmark.

of mitochondrial processes, including generation of the proton motive force as well as apoptosis, mitophagy and mitochondrial fission.[8–13] CL has been identified in structures of both CIII[14,15] and CIV,[16–18] and has been shown to be required for their full activity.[15,19–24] CL has further been suggested to act as a 'glue' between respiratory complexes, stabilising and promoting association of the individual complexes into the so-called supercomplex structures.[25–28]

Supercomplex structures vary in their composition, often comprising a CIII dimer, one or two copies of CIV and, in the case of the so-called 'respirasome', also including complex I (CI; NADH dehydrogenase). *S. cerevisiae* lacks CI,[29] thus the recently resolved $CIII_2CIV_2$ supercomplexes[3,30–32] represent a maximal supercomplex. The CIII:CIV interface differs in these supercomplexes, as compared to those containing CI,[2,33] as is also the case in the first mammalian $CIII_2CIV_1$ structures.[34] In the majority of the $CIII_2CIV_{1-2}$ structures, bound CL is located at the interface between individual complexes[3,31,32,34] and is able to form polar contacts between both CIII and CIV (Fig. 1A).

Previous coarse-grained (CG) MD simulations investigating the CL-dependent assembly of $CIII_2CIV_{1\text{-}2}$ supercomplexes show binding of CL at defined binding sites prior to oligomerisation. Following enrichment of CL on the protein surface, the complexes associate to form an array of supercomplex structures, leading to the suggestion that CL acts to steer and "glue" the individual complexes together.[35] However, the precise molecular mechanism responsible for CL-dependent supercomplex stability and activity is unclear.

Monolysocardiolipin (MLCL) is a CL variant that has only three acyl chains and a hydroxyl group in place of the fourth. Accumulation of MLCL is observed in the mitochondrial membranes of people with Barth syndrome (BTHS).[36] BTHS is caused by a mutation in the tafazzin gene,[37] leading to dysfunctional cardiolipin biosynthesis.[38] Clinical manifestations of BTHS include growth retardation, skeletal muscle fatigue and cardiomyopathy.[39,40] The cellular and molecular basis of BTHS can be attributed to numerous factors, including destabilisation of supercomplexes.[41–44]

In silico investigations into the molecular properties of MLCL shows that the lipid retains an equivalent charge state to CL.[45] However, molecular dynamics (MD) simulations reveal contrasting molecular geometries: MLCL exhibits a more cylindrical shape and in the bilayer the phosphate headgroup containing the lyso hydroxyl tilts itself away from the hydrophobic bilayer core and towards the interfacial region. Furthermore, the acyl chain adjacent to the lyso hydroxyl moiety exhibits increased ordering.[46] These molecular properties likely contribute to the observation that MLCL, unlike CL, does not readily localise to negatively curved regions of the membrane.[46,47] Such alterations of the membrane biophysical properties may impact the activity and stability of membrane-embedded proteins.[48]

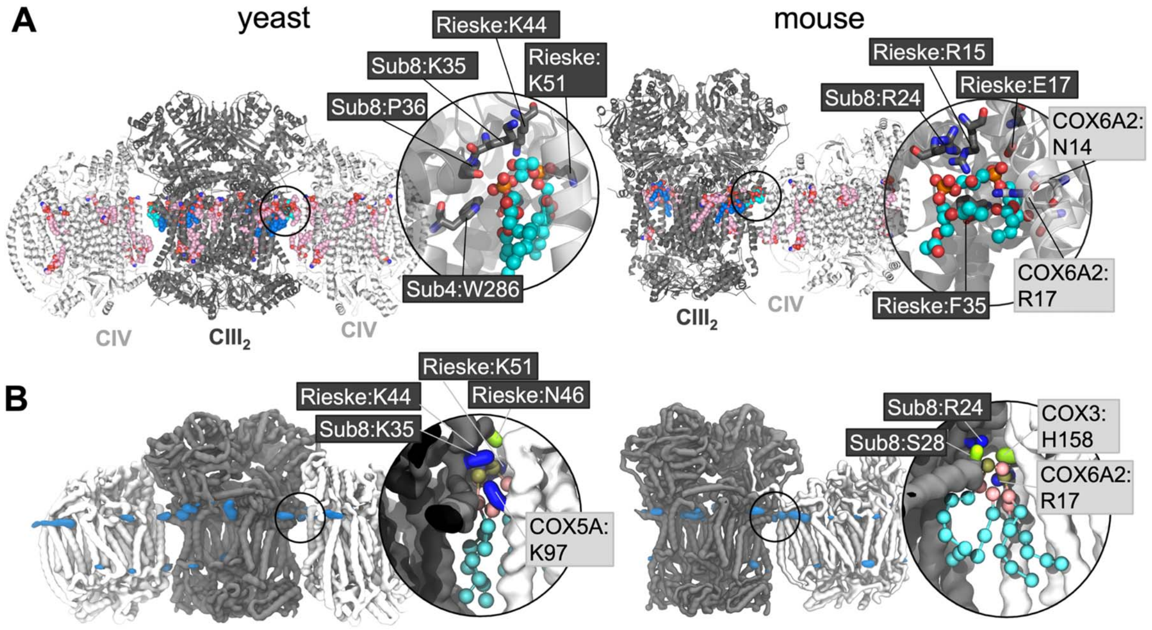

Fig. 1 (A) EM structures of yeast (PDB 6HU9) and mouse (7O3C) supercomplexes, with CL and other bound lipids shown. Non-interface CL are shown in dark blue with the interface CL in cyan; other lipids are in pink. Inset is a close-up of the interface CL, with key coordinating residues shown (for comparison with the CG simulations this is defined as residues within 5 Å of the phosphorous atoms of the phosphate moieties or the C1 atom of the bridging glycerol moieties). Phosphorous atoms are in orange; oxygen in red. Residues are labelled with their subunit and name, with black boxed residues from CIII, and pale grey boxed residues from CIV. (B) CL headgroup density from $CIII_2CIV_2$ CG MD simulations of yeast and murine supercomplexes. Insets show snapshots of CL in the interface interaction site. The backbone is shown of CIII (grey) and CIV (white), with sidechains shown of residues within 5.2 Å of the CL headgroup (the phosphate beads and bridging glycerol); lysine and arginine sidechains in blue, histidine, serine and asparagine in green, and phenylalanine in orange. CL is shown with phosphate moieties in tan, glycerol moieties in pink, and acyl chain beads in cyan.

Early detergent solubilisation studies revealed the reduced affinity of MLCL for CIV.[49] Furthermore, reconstitution of CIV with MLCL retains only 60% of the activity of CL reconstitution. More recently, ^{31}P-NMR spectroscopy was used in tandem with detergent solubilisation to reveal MLCL binds with lower affinity to mitochondrial membrane proteins.[50] However, the mechanism by which the unique molecular properties of MLCL impact on specific protein-lipid interactions to affect stability and functionality remains unclear.[51] Moreover, understanding the role of MLCL accumulation in abnormal supercomplex structure and function remains to be understood.

Here, we use CG and atomistic (AT) MD simulations of the *S. cerevisiae* supercomplex CIII$_2$CIV$_2$ (PDB accession code: 6HU9) and murine supercomplex CIII$_2$CIV (PDB accession code: 7O3C) embedded in a mitochondrial membrane mimetic to characterise the interactions of CL and MLCL with the supercomplex. A CG approach is computationally cost-effective and, compared to conventional atomistic simulations, allows for investigation of protein-lipid interactions on longer, more physiologically relevant, timescales. The CG MD simulations show that CL and MLCL form similar interaction sites on the supercomplex, in particular both lipids form an interaction site at the CIII:CIV interface, also identified in cryo-EM structures. However, free energy perturbation calculations suggest that MLCL interactions are weaker than CL. To offer further insight into differing interaction modes between the lipids, AT MD is used to probe the contribution of each individual respiratory complex to lipid binding, indicating that MLCL forms a weaker interaction with CIV in the interaction site, which appears to destabilise the supercomplex compared to when CL is bound. This supports a role of CL acting as a more effective "glue" to stabilise the interface contacts and overall supercomplex. CG MD of a human CIII$_2$CIV$_1$ supercomplex model demonstrate that the interface site is maintained, bolstering the hypothesis that weaker MLCL interactions at this site could be a mechanism of supercomplex degradation in people with BTHS.

Methods

Structures used

Coordinates for *S. cerevisiae* respiratory supercomplex CIII$_2$CIV$_2$ were taken from PDB ID 6HU9.[31] The murine CIII$_2$CIV$_1$ supercomplex was taken from PDB ID 7O3C.[34] The human CIII$_2$CIV$_1$ supercomplex structures was modelled by alignment of human CIII (PDB ID: 5XTE[52]) and CIV (PDB ID: 5Z62[53]) with the murine supercomplex.[34] All bound lipids were removed before processing.

CG MD simulations

Atomistic protein structures were converted into CG models using MARTINI2.2[54–56] and the martinize. py script (version 2.4; https://md.chem.rug.nl/index.php/tools/proteins-and-bilayers). An elastic network was applied over the complete supercomplex, between BB beads within 1 nm with a force constant of 1000 kJ mol^{-1} nm^{-2}. Protein complexes were embedded in a bilayer of varying lipid ratios and dimensions (Table 1) using insane.py.[57] Standard MARTINI lipid parameters were used for phosphatidyl choline (PC) and phosphatidyl ethanolamine (PE). Tetraoleoyl-CL was taken from ref. 58 while trioleoyl-MLCL was taken from ref. 46.

The CG MD simulations were performed using Gromacs 2020.[59,60] Energy minimisation was performed with the steepest-descent method over 5000 steps. Subsequent two-part equilibration followed. The systems were initially equilibrated for 500 ps with a 10 fs timestep and then for 1000 ps with a 20 fs timestep. Subsequent production simulations (3 × 15 μs for each supercomplex) were run with a 20 fs timestep. For the equilibration, pressure was coupled to a semi-isotropic Berendsen barostat[61] set to 1 bar, and the temperature was maintained at 323 K *via* a velocity-rescale thermostat[62] with a time constant of 1 ps. For the production simulations, pressure was maintained at 1 bar using a Parrinello-Rahman barostat[63] with a coupling time constant of 12 ps, and a compressibility of 3×10^{-4} bar^{-1}. The reaction field coulombic interactions were switched off at 1.1 nm. van der Waals interactions were calculated using a 1.2 nm cut-off with a switching function in place from 0.9 nm. LINCS constraints were applied to covalent bonds.

Free energy perturbation (FEP) calculations

Free energy perturbation (FEP) calculations were performed on the *S. cerevisiae* supercomplex structure with a single CIII monomer and its neighbouring CIV monomer, or on the full murine supercomplex. The starting structure was obtained from a snapshot of a 15 μs simulation where a single CL was bound at the interface position, or at the equivalent non-interface site for the murine supercomplex.

The CL was alchemically perturbed into a MLCL molecule by removing one of the four acyl chains, see ESI.† FEPs were run as previously described.[64] In brief, 21 windows were used to perturb the Lennard-Jones interactions in even sized steps of 0.05. Each window was energy minimised using the steepest descent method and then simulated for 50 ns using the same conditions as for the unbiased simulations. Softcore potentials were applied to the Lennard-Jones interactions using an α of 0.5 and a σ of 0.3. The results were analysed using the alchemical analysis script and implemented a Multistate Bennett acceptance ratio (MBAR) method to calculate the free energy landscape.[65] To obtain a $\Delta G_{\text{binding}}$ value, alchemical transformation was performed both in the binding site (calculating ΔG_{bound}) as well as for a lipid in a membrane with no protein present (calculating ΔG_{free}). This process was repeated five times for both bound and free simulations.

Atomistic MD simulations

The *S. cerevisiae* CIII$_1$CIV$_1$ supercomplex structure with a single CL bound at the CIII:CIV interface was back-mapped from a CG structure into atomistic detail using CG2AT2,[66] with adaptation to include the MLCL topology.[46] The initial CG coordinates were obtained from selecting the final frame of the 25 μs simulation of the CIII$_1$CIV$_1$ supercomplex in a PC : PE membrane with 1 CL at the interface. This simulation was seeded from a bound CL

Table 1 Simulations Performed

Species	Protein	PDB	Lipids	Duration	CG/AT
Yeast	$CIII_2CIV_2$	6HU9	PC : PE : CL (45 : 35 : 20) PC : PE : MLCL (45 : 35 : 20)	3 × 15 μs 3 × 15 μs	CG
Mouse	$CIII_2CIV$	7O3C	PC : PE : CL (45 : 35 : 20) PC : PE : MLCL (45 : 35 : 20)	3 × 15 μs 3 × 15 μs	CG
Human	$CIII_2CIV$	5XTE, 5Z62	PC : PE : CL (45 : 35 : 20) PC : PE : MLCL (45 : 35 : 20)	3 × 15 μs 3 × 15 μs	CG
Yeast	$CIII_1CIV_1$	6HU9	PC : PE (55 : 45) + 1 CL at interface site	1 × 25 μs	CG
Yeast	$CIII_1CIV_1$	6HU9	PC : PE (55 : 45) + 1 CL at interface site PC : PE (55 : 45) + 1 MLCL at interface site	3 × 100 ns 3 × 100 ns	AT
Yeast	$CIII_1CIV_1$	6HU9	PC : PE (50 : 50) + 1 CL at interface site perturbed to MLCL	5 × 20 × 50 ns	CG-FEP
Mouse	$CIII_2CIV$	7O3C	PC : PE (50 : 50) + 1 CL at interface site perturbed to MLCL	5 × 20 × 50 ns	CG-FEP
Mouse	$CIII_2CIV$	7O3C	PC : PE (50 : 50) + 1 CL at non-interface site perturbed to MLCL	5 × 20 × 50 ns	CG-FEP

pose from the main CG simulations, trimmed to a single copy of each CIII and CIV built into a new PC : PE membrane. This was followed by a steepest descent energy minimisation for 50 000 steps. Simulations were performed with GROMACS 2020[59,60] using the CHARMM36m forcefield.[67] Particle Mesh Ewald[68] was used for modelling long-range electrostatics. Pressures were maintained at 1 bar using Parrinello-Rahman barostat[63] with a coupling constant of 2 ps and temperatures at 310 K using a velocity-rescale thermostat[62] and a coupling constant of 0.2 ps. Short range van der Waals and electrostatics were cut-off at 1.2 nm and bonds were constrained using the LINCS algorithm.[69]

Analysis

Analysis was performed using inbuilt tools provided by GROMACS 2020,[59,60] VMD,[70] and MDAnalysis.[71,72] The VMD plugin VolMap was used for initial assessment of lipid interaction sites, using a resolution of 2 Å for the grid and particle size 3× the particle radius. Densities were calculated for all frames and combined using the mean. Lipid binding sites were identified and the kinetics of dissociation were assessed using PyLipID.[73] Visualisation and image generation was carried out using VMD[70] and PyMOL.

Results

To investigate CL and MLCL interaction with mitochondrial supercomplexes, 3 × 15 μs CG MD simulations were run of yeast and mammalian $CIII_2CIV_{1\text{-}2}$ supercomplex structures, in bilayers containing PC, PE and either CL or MLCL.

CL and MLCL interact at sites identified experimentally

Volumetric maps assessing the average weighted density of each lipid's phosphate beads reveal defined lipid binding sites for both CL (Fig. 1B) and MLCL (Fig. S1†). Areas of lipid density are observed in the inner cavity of CIII, which is known to be highly hydrophobic, and contains PC, PE and CL in cryo-EM structures (Fig. 1A). The areas of lipid occupancy that do not correspond to bound CL in the cryo-EM structure are generally located on the protein surface exposed to the membrane, and therefore are more susceptible to removal during protein purification procedures.

CL and MLCL interact at the CIII:CIV interface

Lipid density is observed at the interface region between CIII and CIV (Fig. 1B), in the same region that a bound CL lipid was identified in the cryo-EM yeast and murine structures (Fig. 1A).

To gain more detailed insights into this site, the CG data were analysed using the PyLipID program, which groups protein residues into binding sites by clustering residues that frequently interact simultaneously with the same lipid molecule.[73] For the yeast supercomplex, PyLipID identifies a number of sites including a very high occupancy site at the interface region (Table 2 and S1†). This site contains three lysine residues from CIII (Rieske subunit K44, K51; Subunit 8 K35), a lysine from CIV (COX5A K97) and several polar residues from both CIII and CIV (Fig. 1B and Table 2), which interact with the CL headgroup (*i.e.* phosphate groups and bridging glycerol). For the murine supercomplex, PyLipID also identifies a high occupancy site at this interface region, which contains an arginine from CIII (Subunit 8 R24), two arginines and a lysine from CIV (COX3 R156, COX6A2 R17, COX7A2L K56), and several polar residues from both (Table 2 and S1†). Sequence alignment of yeast and murine supercomplexes show that residues on subunit 8 of CIII that interact with CL are well-conserved (Fig. S3, S4 and S5†).

In simulations where CL was replaced by MLCL (Fig. 2A), analysis using both volumetric maps and PyLipID also identified the interface interaction site as being a site for the MLCL headgroup (Fig. 2B, S1† and Table 2), indicating that both CL and MLCL are able to bind the interface site.

CL interacts more favourably than MLCL at the interface site

Given that the presence of MLCL in place of CL is thought to destabilise these supercomplexes, we reasoned that the site identified on the interface between CIII and CIV might be of physiological relevance. Therefore, free energy perturbation

Table 2 Residues identified in the interface interaction site as identified by PyLipID. All residues with occupancy of >40% are listed. Note that the yeast supercomplex, due to having two CIV monomers, also has two interface interaction sites

Species	Lipid	Residues
Yeast	CL	Site 1: CIII: *Rieske subunit*: K44, K51; *Sub8*: K35; *Sub9*: S2, F3, S4, S5 CIV: *COX5A*: S93, F94, K97 Site 2: CIII: *Rieske subunit*: K44, K51, Y55; *Sub8*: K35, P36, L37; *Sub9*: S2, S4, S5 CIV: *COX5A*: S93, K97
	MLCL	Site 1: CIII: *Rieske subunit*: K44, N46, K51; *Sub8*: K35 CIV: *COX1*: K408; *COX5A*: G90, S93, K97 Site 2: CIII: *Rieske subunit*: K44, N46, K51, Y55; *Sub8*: K35, P36, L37, Q38, H42 CIV: *COX5A*: G90, S92, S93, F94, K97
Mouse	CL	CIII: *Sub8*: R24, F26, S28, S31 CIV: *COX7A2L*: S54, G55, K56; *COX3*: R156, N157, H158, Q161, L223; *COX5B*: S3; *COX6A2*: R17
	MLCL	CIII: *Sub8*: R24, S31 CIV: *COX7A2L*: Y53, S54, G55, K56; *COX3*: R156, N157, H158, N160, L223; *COX5B*: S3
Human	CL	CIII: *Rieske subunit*: R93, F113; *Sub4*: T305, H309; *Sub8*: R25, A26, Y27, P28, H29, V30, T32 CIV: *COX3*: N157, Q158; *COX5B*: A32; *COX6A1*: R36, K39
	MLCL	CIII: *Rieske subunit*: R93, F113; *Sub4*: T305, H309; *Sub8*: R25, A26, Y27, P28, H29, V30, T32 CIV: *COX3*: N157, Q158, Q161; *COX5B*: A32; *COX6A1*: R36, K39

(FEP) calculations were used to characterise the binding energies of CL and MLCL to the protein interface site.

To identify the relative difference in binding affinity of CL and MLCL for the interface site, FEPs were performed in which CL was alchemically transformed into MLCL (Fig. S2†) both bound to the protein and free in the membrane. The ΔG associated with transformation of protein-bound CL into MLCL was higher than the ΔG for transformation in the bulk bilayer, suggesting that CL interacts with the protein interface site more favourably than MLCL, with a $\Delta\Delta G$ value calculated at 7 kJ mol^{-1} (Fig. 2C). This is roughly equivalent to the binding strength of CL to certain other proteins,[74] suggesting that it is a substantial difference.

Presence of CIV determines preference for CL at interface site

The murine supercomplex contains only one copy of CIV, but two copies of CIII (an obligate dimer). Thus, there will be one CIII:CIV interface site, but also a site in the equivalent position on the other CIII monomer, where no neighbouring CIV is present, which we term the 'non-interface site'. PyLipID identifies the non-interface site as a lipid binding site. However FEP calculations show that at the non-interface site the preference for CL over MLCL is no longer apparent (Fig. 2C). This suggests that CIV is important in providing the preference for CL *vs.* MLCL at the interface site.

CL makes more contacts than MLCL with CIV at the interface site

In order to further understand the importance of CIV for the interface site, atomistic simulations of the CIII : CIV interface with a single CL or MLCL molecule were performed. Snapshots from the simulations indicate that the four acyl chains of CL may be able to form more extensive contacts with CIV than is possible for MLCL with only three acyl chains (Fig. 3A and B). Contact analysis shows that the number of CIII-lipid contacts are similar for CL and MLCL (Fig. 3C). However, MLCL makes

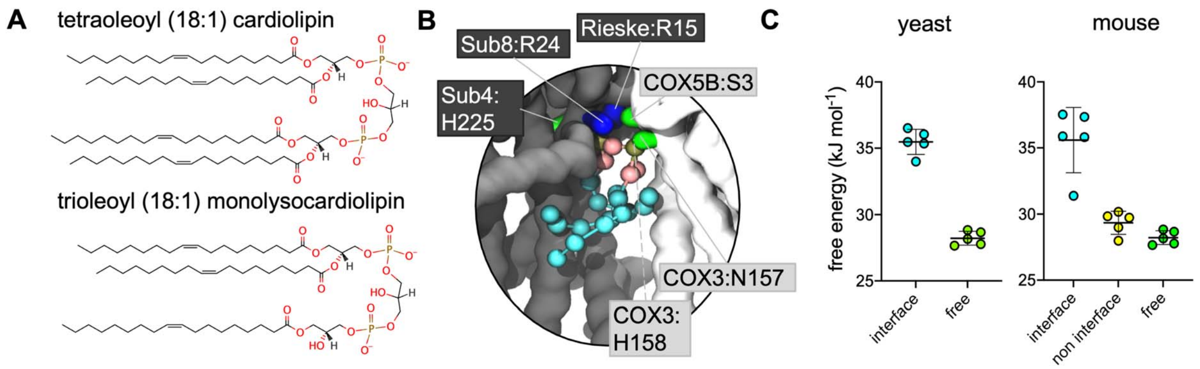

Fig. 2 (A) Structures of CL and MLCL used for this study. (B) CG MLCL pose used for free energy perturbation (FEP) demonstrating MLCL interaction in the murine supercomplex interface. Protein residues within 5.2 Å of the MLCL headgroup (phosphate and bridging glycerol beads) have sidechains shown. (C) CG FEP of CL *vs.* MLCL in yeast and mouse (the latter has equivalent interface and non-interface sites). $\Delta\Delta G$ values are 7 kJ mol^{-1} for both the yeast and the mouse interface site (*i.e.* CL binds more strongly than MLCL), and 1 kJ mol^{-1} for the mouse non-interface site.

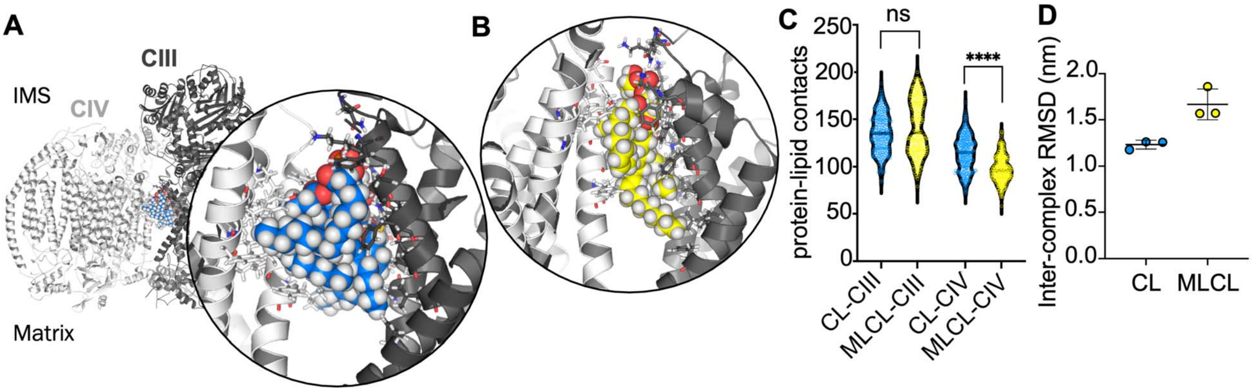

Fig. 3 (A) Atomistic yeast supercomplex with interface cardiolipin shown in blue. Inset, all protein residues within 4 Å of the CL are shown as sticks. (B) Atomistic simulation of the yeast supercomplex with MLCL, shown in yellow. MLCL makes fewer contacts with CIV (white) than CIII (grey). (C) Number of contacts made in atomistic simulations between CIII or CIV and either CL or MLCL. CL and MLCL make similar contacts to CIII (median atoms in contact are 134 and 137), whereas MLCL makes significantly fewer contacts to CIV. To obtain statistics for the data, we resampled each distribution using 50 rounds of bootstrapping. These were then used to compare each condition. Comparing CL-CIII *vs.* MLCL-CIII gives a non-significant ($p = 0.1451$) difference in means, of 134.0 to 137.7. Comparing CL-CIV *vs.* MLCL-CIV gives a strongly-significant ($p < 0.0001$) difference in means of 114.9 to 98.12 (D) RMSD of CIV, when the entire yeast supercomplex is fitted to CIII, in the presence of either CL or MLCL. The lower RMSD suggests that CL (1.2 ± 0.0 nm) stabilises the complex more than MLCL (1.7 ± 0.2 nm).

significantly fewer contacts with CIV than CL does. The size of the simulations (*ca.* 760 000 atoms) limit sampling to 3 × 100 ns per condition, therefore caution should be used in interpreting these results, however, this suggests that the preference for CL *vs.* MLCL in the interface site is driven by a greater number of CIV-acyl chain interactions for CL as compared to MLCL, which supports the conclusions from the free energy analyses. Furthermore, when fitting the entire complex to CIII over the course of each simulation, the RMSD of CIV is lower in the presence of CL than MLCL (Fig. 3D). While caution should be taken in interpreting RMSDs for a simulations of 100 ns, this suggests that CL stabilises the supercomplex more than MLCL.

Interface site identified in a human model of $CIII_2CIV_1$

In order to confirm that the lipid interaction site at the CIII:CIV interface could indeed be relevant for BTHS, we ran CG MD simulations of a model of the human $CIII_2CIV_1$ supercomplex. Whilst a structure of the human respirasome has been resolved (*ie*. containing CI as well as CIII and CIV) no structure of the $CIII_2CIV_1$ exists to our knowledge. Therefore, we built a model based on human CIII and CIV structures[52,53] superposed on the murine supercomplex.[34] Analysis using VolMap (Fig. 4A) and PyLipID (Fig. 4B) again identified the interface interaction site. As for the yeast and murine complexes, the human interface interaction site contains two arginine residues from CIII and a further positively charged residue on CIV (Fig. 4B and Table 2).

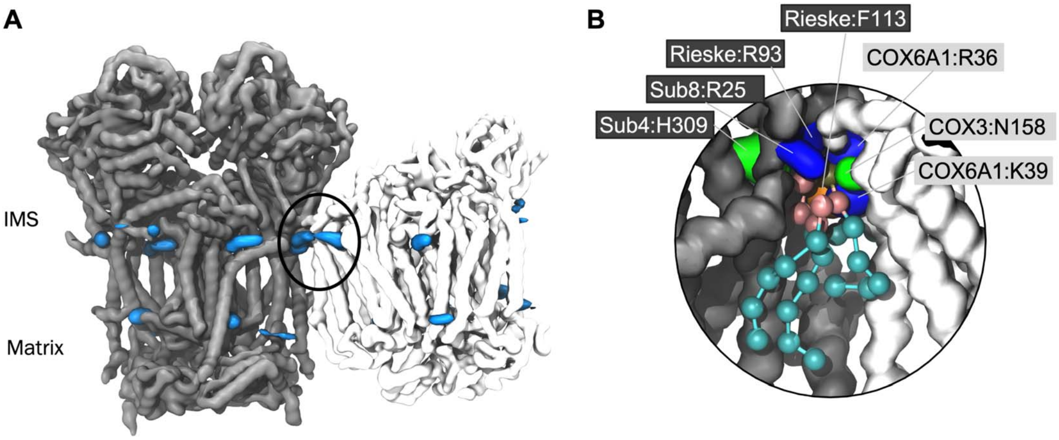

Fig. 4 (A) CL headgroup density from human $CIII_2CIV_1$ CG MD simulations. CIII backbone is shown in grey and CIV in white, with CL headgroup densities in blue. (B) Snapshot of CL in the human supercomplex interface interaction site (location circled in A). Protein residues within 5.2 Å of CL headgroup have sidechains shown. CL is shown with phosphate moieties in tan, glycerol moieties in pink, and acyl chain beads in cyan. The backbone is shown of CIII (grey) and CIV (white), with sidechains shown of residues within 5.2 Å of the CL headgroup; lysine and arginine sidechains in blue, histidine and asparagine in green, and phenylalanine in orange.

Identification of the interface lipid interaction site suggests that the interaction of CL and MLCL in the human supercomplex may be similar to that seen in yeast and murine supercomplexes.

Discussion

CL and MLCL association with the mitochondrial supercomplex $CIII_2CIV_{1-2}$

The association of CL with respiratory complexes and supercomplexes is well-documented.[75] MLCL has been shown to interact with CIV but with a lower affinity than CL[49] and reconstitution of both CIV and the ATP/ADP transporter with MLCL rather than CL lead to reduced protein activity.[49,76] However, there has been less investigation into the protein-lipid interactions of supercomplexes and MLCL. Here, we have shown that both CL and MLCL show enrichment at defined binding sites, consistent with sites identified previously in cryo-EM structures and MD simulations focussed on the individual respiratory complexes.[77,78]

Both CL and MLCL appear to show greater enrichment in the matrix-facing leaflet compared to the inter membrane space (IMS)-facing leaflet. This is likely due to the physiological distribution of CL in the inner mitochondrial membrane in which it represents up to 20% of the matrix-facing leaflet and presents substantial paucity in the IMS-facing leaflet,[7] an observation which is also apparent in bacterial proteins.[79] Therefore, it is plausible that functionally significant CL binding would have evolved to occur in the matrix-facing side of the supercomplex protein.

CL and MLCL interaction at the CIII:CIV interface site

The interface site is formed of a cluster of positively charged residues, alongside several polar residues. The CL glycerol moieties that connect phosphate groups with acyl tails also interact with aromatic groups such as yeast W286 on subunit 4 of CIII, and murine F35 on the Rieske subunit of CIII (see for comparison Fig. 1A). Together these interactions form all the characteristic features of bacterial CL interaction sites as we previously identified[79] suggesting a conserved mode of binding.

The CL interface site is conserved across yeast, mouse and human $CIII_2CIV_{1\text{-}2}$ supercomplexes (Fig. 1, 4 and S1) indicating functional importance. The site is also conserved for MLCL, which has a similar chemical composition to that of CL. It has been suggested that lipid enrichment at interface sites between complexes may be responsible for "gluing" the complexes together,[25,77] and extending the minimal protein–protein interaction surface area.[26] For this mechanism to be effective, the lipid would be required to bridge both complexes stably. Analysis of our atomistic data suggests that, when bound to the interface site, CL forms more contacts with CIV, but no difference in the number of contact with CIII (Fig. 4B). Residues interacting with the lipid headgroups do not differ greatly for CL and MLCL, thus the difference in interactions may be attributed to the extra acyl chain of CL, which leads to CL exhibiting a more conical shape than MLCL. CL may therefore be able to maximise supercomplex stability by bridging the two protein surfaces. Indeed, analysis of our atomistic MD data appears to support this (Fig. 3D).

FEP calculations of the interface site *vs.* the equivalent non-interface site on the other CIII monomer (Fig. 3C) suggest that the presence of CIV contributes to the relative strength of association of CL interaction *vs.* that of MLCL. This is likely due to a lack of defined bridging interactions across the interface for MLCL, which may also influence the supercomplex stability, as described above. Additionally, this suggests that CL is likely to spend more time at the interface site than MLCL, therefore provide more stability to the supercomplex over long timescales.

Interestingly, previous PMF calculations indicate CL and MLCL exhibit identical free energies of binding to a CIV binding site proposed to be involved in supercomplex interface oligomerisation.[35] Along with our data, this suggests that it is only in the context of the supercomplex, where there is an interface site, that the difference between MLCL and CL can be observed.

MD simulations show CL enrichment at interface sites on individual respiratory complexes prior to oligomerisation into supercomplex structures.[35] Furthermore, the site on CIII has been identified in previous simulations of only the CIII dimer (site III in ref. 77), and the CIV component of the interface site has also been observed in simulations of CIV alone (site V in ref. 78), perhaps indicating that CL interaction precedes supercomplex formation. However, recent work has shown that supercomplex assembly may happen in tandem with assembly of the individual complexes,[80] rather than proceeding after assembly of constituent components. Thus, it is unclear whether CL helps to guide supercomplex assembly, or functions principally to stabilise existing supercomplexes.

Limitations

This work does not account for CL in all supercomplex variants; other supercomplexes (in particular the mammalian respirasome, containing CI as well as $CIII_2$ and CIV[52,81–84]) have a different CIII:CIV interface: where CIII interacts with CIV in $CIII_2CIV_{1-2}$, instead CIII instead forms an interaction with CI. Furthermore, in the recently structurally resolved $CICIICIII_2$-CIV_2 ciliate supercomplex, there is no CIII:CIV interface at all.[85] Thus, the interface lipid sites will be different, although the same mechanism for weaker MLCL interaction is conceivable.

In addition, our study is limited to CL and MLCL with oleyl tails. This is a matter of necessity, as sampling all possible combinations of tails would be a difficult prospect. Future work might do well to investigate how different lipid tails effect the findings presented here.

In this study, we show that MLCL interacts less favourably than CL in the supercomplex interface interaction site. Our results support the hypothesis that CL glues the respiratory complexes together more effectively than MLCL,[25,26,28] and are in agreement with data showing that MLCL does not bind as tightly to mitochondrial proteins.[50] Future work might look at directly measuring the free energy of interaction between CIII and CIV in the presence of CL, MLCL or another lipid.

Conclusions

Our results provide molecular understanding on the lack of supercomplexes in BTHS, where MLCL accumulates and mature CL is depleted. While the role of supercomplexes remains to be fully understood, the results presented here demonstrate the importance of specific lipid interactions in supercomplexes, and pinpoint how a relatively minor change to a lipid species might have system-wide implications, such as in BTHS.

Data availability

Structure and trajectory files for all the coarse-grained and atomistic simulations analysed in this article are available at zenodo: **https://zenodo.org/record/7261108#.Y1u6N0pByEA** (**https://doi.org/10.5281/zenodo.7261108**).

Author contributions

Conceptualisation: A. L. D.; validation: R. A. C., N. H.; formal analysis: R. A. C., N. H.; investigation: R. A. C., N. H.; provision of computing resources: P. J. S., M. S. P. S.; data curation: R. A. C., A. L. D.; writing – original draft preparation: R. A. C., N. H., A. L. D.; writing – review & editing: R. A. C., N. H., P. J. S., M. S. P. S., A. L. D.; visualization: R. A. C., N. H., A. L. D.; supervision: R. A. C., A. L. D.; project administration: A. L. D.; funding acquisition: P. J. S., M. S. P. S.

Conflicts of interest

There are no conflicts of interest to declare.

Acknowledgements

R. A. C., A. L. D., P. J. S., and M. S. P. S. are funded by Wellcome (208361/Z/17/Z). A. L. D. was also supported by the Department of Biochemistry, University of Oxford. Research in M. S. P. S.'s group is also supported by BBSRC (BB/R00126X/1) and EPSRC (EP/R004722/1). Research in P. J. S.'s laboratory is funded by the MRC (MR/S009213/1) and BBSRC (BB/P01948X/1, BB/R002517/1, and BB/S003339/1). Simulations were carried out, in part, on ARCHER, provided by HECBioSim, the UK High End Computing Consortium for Biomolecular Simulation (hecbiosim.ac.uk), which is supported by the EPSRC (EP/R029407/1). We would like to thank Dr Irfan Alibay and Dr Michael Horrell for the maintenance of local computing resources. For the purpose of Open Access, the author has applied a CC BY public copyright licence to any Author Accepted Manuscript version arising from this submission.

References

1 F. Calisto, F. M. Sousa, F. V. Sena, P. N. Refojo and M. M. Pereira, Mechanisms of energy transduction by charge translocating membrane proteins, *Chem. Rev.*, 2021, **121**, 1804–1844.

2 P. Brzezinski, A. Moe and P. Ädelroth, Structure and mechanism of respiratory III-IV supercomplexes in bioenergetic membranes, *Chem. Rev.*, 2021, **121**, 9644–9673.

3 J. Berndtsson, *et al.*, Respiratory supercomplexes enhance electron transport by decreasing cytochrome *c* diffusion distance, *EMBO Rep.*, 2020, **21**, e51015.

4 A. Moe, J. Di Trani, J. L. Rubinstein and P. Brzezinski, Cryo-EM structure and kinetics reveal electron transfer by 2D diffusion of cytochrome *c* in the yeast III-IV respiratory supercomplex, *Proc. Natl. Acad. Sci. U. S. A.*, 2021, **118**, e2021157118.

5 J. N. Blaza, R. Serreli, A. J. Y. Jones, K. Mohammed and J. Hirst, Kinetic evidence against partitioning of the ubiquinone pool and the catalytic relevance of respiratory-chain supercomplexes, *Proc. Natl. Acad. Sci. U. S. A.*, 2014, **111**, 15735–15740.

6 M. Schlame, Protein crowding in the inner mitochondrial membrane, *Biochim. Biophys. Acta, Bioenerg.*, 2021, **1862**, 148305.

7 S. E. Horvath and G. Daum, Lipids of mitochondria, *Prog. Lipid Res.*, 2013, **52**, 590–614.

8 G. Paradies, *et al.*, Functional role of cardiolipin in mitochondrial bioenergetics, *Biochim. Biophys. Acta, Bioenerg.*, 2014, **1837**, 408–417.

9 C. T. Chu, *et al.*, Cardiolipin externalization to the outer mitochondrial membrane acts as an elimination signal for mitophagy in neuronal cells, *Nat. Cell Biol.*, 2013, **15**, 1197–1205.

10 J. Dagvadorj, *et al.*, Recruitment of pro-IL-1α to mitochondrial cardiolipin, *via* shared LC3 binding domain, inhibits mitophagy and drives maximal NLRP3 activation, *Proc. Natl. Acad. Sci. U. S. A.*, 2021, **118**, e2015632118.

11 D. Mohammadyani, *et al.*, Structural characterization of cardiolipin-driven activation of cytochrome *c* into a peroxidase and membrane perturbation, *Biochim. Biophys. Acta, Biomembr.*, 2018, **1860**, 1057–1068.

12 T. Ban, *et al.*, Molecular basis of selective mitochondrial fusion by heterotypic action between OPA1 and cardiolipin, *Nat. Cell Biol.*, 2017, **19**, 856–863.

13 M. Mahajan, *et al.*, NMR identification of a conserved Drp1 cardiolipin-binding motif essential for stress-induced mitochondrial fission, *Proc. Natl. Acad. Sci. U. S. A.*, 2021, **118**, e2023079118.

14 H. Palsdottir, C. G. Lojero, B. L. Trumpower and C. Hunte, Structure of the yeast cytochrome bc_1 complex with a hydroxyquinone anion Q_o site inhibitor bound, *J. Biol. Chem.*, 2003, **278**, 31303–31311.

15 C. Lange, J. H. Nett, B. L. Trumpower and C. Hunte, Specific roles of protein-phospholipid interactions in the yeast cytochrome bc_1 complex structure, *EMBO J.*, 2001, **20**, 6591–6600.

16 L. Qin, C. Hiser, A. Mulichak, R. M. Garavito and S. Ferguson-Miller, Identification of conserved lipid/detergent-binding sites in a high-resolution structure of the membrane protein cytochrome *c* oxidase, *Proc. Natl. Acad. Sci. U.S.A.*, 2006, **103**, 16117–16122.

17 K. Shinzawa-Itoh, *et al.*, Structures and physiological roles of 13 integral lipids of bovine heart cytochrome *c* oxidase, *EMBO J.*, 2007, **26**, 1713–1725.

18 S. Yoshikawa, K. Muramoto, K. Shinzawa-Itoh and M. Mochizuki, Structural studies on bovine heart cytochrome *c* oxidase, *Biochim. Biophys. Acta*, 2012, **1817**, 579–589.

19 M. Fry and D. E. Green, Cardiolipin requirement for electron transfer in complex I and III of the mitochondrial respiratory chain, *J. Biol. Chem.*, 1981, **256**, 1874–1880.

20 B. Gomez and N. C. Robinson, Phospholipase digestion of bound cardiolipin reversibly inactivates bovine cytochrome bc_1, *Biochemistry*, 1999, **38**, 9031–9038.

21 N. C. Robinson, F. Strey and L. Talbert, Investigation of the essential boundary layer phospholipids of cytochrome *c* oxidase using Triton X-100 delipidation, *Biochemistry*, 1980, **19**, 3656–3661.

22 M. Fry and D. E. Green, Cardiolipin requirement by cytochrome oxidase and the catalytic role of phospholipid, *Biochem. Biophys. Res. Commun.*, 1980, **93**, 1238–1246.

23 S. B. Vik, G. Georgevich and R. A. Capaldi, Diphosphatidylglycerol is required for optimal activity of beef heart cytochrome *c* oxidase, *Proc. Natl. Acad. Sci. U. S. A.*, 1981, **78**, 1456–1460.

24 N. C. Robinson, Functional binding of cardiolipin to cytochrome *c* oxidase, *J. Bioenerg. Biomembr.*, 1993, **25**, 153–163.

25 M. Zhang, E. Mileykovskaya and W. Dowhan, Gluing the respiratory chain together. Cardiolipin is required for supercomplex formation in the inner mitochondrial membrane, *J. Biol. Chem.*, 2002, **277**, 43553–43556.

26 K. Pfeiffer, *et al.*, Cardiolipin stabilizes respiratory chain supercomplexes, *J. Biol. Chem.*, 2003, **278**, 52873–52880.

27 S. Bazán, *et al.*, Cardiolipin-dependent reconstitution of respiratory supercomplexes from purified *Saccharomyces cerevisiae* complexes III and IV, *J. Biol. Chem.*, 2013, **288**, 401–411.

28 E. Mileykovskaya and W. Dowhan, Cardiolipin-dependent formation of mitochondrial respiratory supercomplexes, *Chem. Phys. Lipids*, 2014, **179**, 42–48.

29 T. Joseph-Horne, D. W. Hollomon and P. M. Wood, Fungal respiration: A fusion of standard and alternative components, *Biochim. Biophys. Acta, Bioenerg.*, 2001, **1504**, 179–195.

30 S. Rathore, *et al.*, Cryo-EM structure of the yeast respiratory supercomplex, *Nat. Struct. Mol. Biol.*, 2019, **26**, 50–57.

31 A. M. Hartley, *et al.*, Structure of yeast cytochrome *c* oxidase in a supercomplex with cytochrome bc_1, *Nat. Struct. Mol. Biol.*, 2019, **26**, 78–83.

32 A. M. Hartley, B. Meunier, N. Pinotsis and A. Maréchal, Rcf2 revealed in cryo-EM structures of hypoxic isoforms of mature mitochondrial III-IV supercomplexes, *Proc. Natl. Acad. Sci. U. S. A.*, 2020, **117**, 9329–9337.

33 J. S. Sousa and J. Vonck, Respiratory supercomplexes III_2IV_2 come into focus, *Nat. Struct. Mol. Biol.*, 2019, **26**, 87–89.

34 I. Vercellino and L. A. Sazanov, Structure and assembly of the mammalian mitochondrial supercomplex $CIII_2CIV$, *Nature*, 2021, **598**, 364–367.

35 C. Arnarez, S. J. Marrink and X. Periole, Molecular mechanism of cardiolipin-mediated assembly of respiratory chain supercomplexes, *Chem. Sci.*, 2016, **7**, 4435–4443.

36 F. Valianpour, *et al.*, Monolysocardiolipins accumulate in Barth syndrome but do not lead to enhanced apoptosis, *J. Lipid Res.*, 2005, **46**, 1182–1195.

37 S. Bione, *et al.*, A novel X-linked gene, *G4.5.* is responsible for Barth syndrome, *Nat. Genet.*, 1996, **12**, 385–389.

38 M. Schlame and M. Ren, Barth syndrome, a human disorder of cardiolipin metabolism, *FEBS Lett.*, 2006, **580**, 5450–5455.

39 P. G. Barth, *et al.*, An X-linked mitochondrial disease affecting cardiac muscle, skeletal muscle and neutrophil leucocytes, *J. Neurol. Sci.*, 1983, **62**, 327–355.

40 R. I. Kelley, *et al.*, X-linked dilated cardiomyopathy with neutropenia, growth retardation, and 3-methylglutaconic aciduria, *J. Pediatr.*, 1991, **119**, 738–747.

41 M. McKenzie, M. Lazarou, D. R. Thorburn and M. T. Ryan, Mitochondrial respiratory chain supercomplexes are destabilized in Barth Syndrome patients, *J. Mol. Biol.*, 2006, **361**, 462–469.

42 F. Gonzalvez, *et al.*, Barth syndrome: Cellular compensation of mitochondrial dysfunction and apoptosis inhibition due to changes in cardiolipin remodeling linked to tafazzin (TAZ) gene mutation, *Biochim. Biophys. Acta*, 2013, **1832**, 1194–1206.

43 J. Dudek, *et al.*, Cardiolipin deficiency affects respiratory chain function and organization in an induced pluripotent stem cell model of Barth syndrome, *Stem Cell Res.*, 2013, **11**, 806–819.

44 I. A. Chatzispyrou, *et al.*, Barth syndrome cells display widespread remodeling of mitochondrial complexes without affecting metabolic flux distribution, *Biochim. Biophys. Acta, Mol. Basis Dis.*, 2018, **1864**, 3650–3658.

45 M. Sathappa and N. N. Alder, The ionization properties of cardiolipin and its variants in model bilayers, *Biochim. Biophys. Acta*, 2016, **1858**, 1362–1372.

46 K. J. Boyd, N. N. Alder and E. R. May, Molecular dynamics analysis of cardiolipin and monolysocardiolipin on bilayer properties, *Biophys. J.*, 2018, **114**, 2116–2127.

47 M. Dahlberg, Polymorphic phase behavior of cardiolipin derivatives studied by coarse-grained molecular dynamics, *J. Phys. Chem. B*, 2007, **111**, 7194–7200.

48 E. R. Pennington, K. Funai, D. A. Brown and S. R. Shaikh, The role of cardiolipin concentration and acyl chain composition on mitochondrial inner membrane molecular organization and function, *Biochim. Biophys. Acta, Mol. Cell Biol. Lipids*, 2019, **1864**, 1039–1052.

49 N. C. Robinson, J. Zborowski and L. H. Talbert, Cardiolipin-depleted bovine heart cytochrome *c* oxidase: binding stoichiometry and affinity for cardiolipin derivatives, *Biochemistry*, 1990, **29**, 8962–8969.

50 Y. Xu, *et al.*, Loss of protein association causes cardiolipin degradation in Barth syndrome, *Nat. Chem. Biol.*, 2016, **12**, 641–647.

51 A. L. Duncan, Monolysocardiolipin (MLCL) interactions with mitochondrial membrane proteins, *Biochem. Soc. Trans.*, 2020, **48**, 993–1004.

52 R. Guo, S. Zong, M. Wu, J. Gu and M. Yang, Architecture of human mitochondrial respiratory megacomplex $I_2III_2IV_2$, *Cell*, 2017, **170**, 1247–1257.

53 S. Zong, *et al.*, Structure of the intact 14-subunit human cytochrome *c* oxidase, *Cell Responses*, 2018, **28**, 1026–1034.

54 S. J. Marrink, H. J. Risselada, S. Yefimov, D. P. Tieleman and A. H. de Vries, The MARTINI force field: Coarse grained model for biomolecular simulations, *J. Phys. Chem. B*, 2007, **111**, 7812–7824.

55 L. Monticelli, *et al.*, The MARTINI coarse-grained force field: Extension to proteins, *J. Chem. Theory Comput.*, 2008, **4**, 819–834.

56 D. H. de Jong, *et al.*, Improved parameters for the Martini coarse-grained protein force field, *J. Chem. Theory Comput.*, 2012, **9**, 687–697.

57 T. A. Wassenaar, H. I. Ingólfsson, R. A. Böckmann, D. P. Tieleman and S. J. Marrink, Computational lipidomics with insane: A versatile tool for generating custom membranes for molecular simulations, *J. Chem. Theory Comput.*, 2015, **11**, 2144–2155.

58 M. Dahlberg and A. Maliniak, Mechanical properties of coarse-grained bilayers formed by cardiolipin and zwitterionic lipids, *J. Chem. Theory Comput.*, 2010, **6**, 1638–1649.

59 H. J. C. Berendsen, D. V. D. Spoel and R. van Drunen, GROMACS: A message-passing parallel molecular dynamics implementation, *Comput. Phys. Commun.*, 1995, **91**, 43–56.

60 D. V. D. Spoel, *et al.*, GROMACS: fast, flexible, and free, *J. Comput. Chem.*, 2005, **26**, 1701–1718.

61 H. J. C. Berendsen, J. P. M. Postma, W. F. Van Gunsteren, A. Dinola and J. R. Haak, Molecular dynamics with coupling to an external bath, *J. Chem. Phys.*, 1984, **81**, 3684–3690.

62 G. Bussi, D. Donadio and M. Parrinello, Canonical sampling through velocity rescaling, *J. Chem. Phys.*, 2007, **126**, 014101.

63 M. Parrinello and A. Rahman, Polymorphic transitions in single crystals: A new molecular dynamics method, *J. Appl. Phys.*, 1981, **52**, 7182–7190.

64 R. A. Corey, O. N. Vickery, M. S. P. Sansom and P. J. Stansfeld, Insights into membrane protein–lipid interactions from free energy calculations, *J. Chem. Theory Comput.*, 2019, **15**, 5727–5736.

65 P. V. Klimovich, M. R. Shirts and D. L. Mobley, Guidelines for the analysis of free energy calculations, *J. Comput.-Aided Mol. Des.*, 2015, **29**, 397–411.

66 O. N. Vickery and P. J. Stansfeld, CG2AT2: An enhanced fragment-based approach for serial multi-scale molecular dynamics simulations, *J. Chem. Theory Comput.*, 2021, **17**, 6472–6482.

67 R. B. Best, *et al.*, Optimization of the additive CHARMM all-atom protein force field targeting improved sampling of the backbone ϕ, ψ and side-chain χ_1 and χ_2 dihedral angles, *J. Chem. Theory Comput.*, 2012, **8**, 3257–3273.

68 T. Darden, D. York and L. Pedersen, Particle mesh Ewald: An $N \cdot \log(N)$ method for Ewald sums in large systems, *J. Chem. Phys.*, 1993, **98**, 10089–10092.

69 B. Hess, H. Bekker, H. J. C. Berendsen and J. G. E. M. Fraaije, LINCS: a linear constraint solver for molecular simulations, *J. Comput. Chem.*, 1997, **18**, 1463–1472.

70 W. Humphrey, A. Dalke and K. Schulten, VMD: visual molecular dynamics, *J. Mol. Graphics*, 1996, **14**(1), 33–38.

71 N. Michaud-agrawal, E. J. Denning, T. B. Woolf and O. Beckstein, MDAnalysis: a toolkit for the analysis of molecular dynamics simulations, *J. Comput. Chem.*, 2011, **32**, 2319–2327.

72 R. Gowers, *et al.*, MDAnalysis: A python package for the rapid analysis of molecular dynamics simulations, *Proc. 15th Python Sci. Conf.*, 2016, 98–105, DOI: **10.25080/majora-629e541a-00e**.

73 W. Song, *et al.*, PyLipID: a python package for analysis of protein–lipid interactions from molecular dynamics simulations, *J. Chem. Theory Comput.*, 2022, **18**, 1188–1201.

74 R. A. Corey, P. J. Stansfeld and M. S. P. Sansom, The energetics of protein–lipid interactions as viewed by molecular simulations, *Biochem. Soc. Trans.*, 2020, **48**, 25–37.

75 A. Musatov and E. Sedlák, Role of cardiolipin in stability of integral membrane proteins, *Biochimie*, 2017, **142**, 102–111.

76 B. Hoffmann, A. Stöckl, M. Schlame, K. Beyer and M. Klingenberg, The reconstituted ADP/ATP carrier activity has an absolute requirement for cardiolipin as shown in cysteine mutants, *J. Biol. Chem.*, 1994, **269**, 1940–1944.

77 C. Arnarez, J. Mazat, J. Elezgaray, S. J. Marrink and X. Periole, Evidence for cardiolipin binding sites on the membrane-exposed surface of the cytochrome bc_1, *J. Am. Chem. Soc.*, 2013, **135**, 3112–3120.

78 C. Arnarez, S. J. Marrink and X. Periole, Identification of cardiolipin binding sites on cytochrome *c* oxidase at the entrance of proton channels, *Sci. Rep.*, 2013, **3**, 1263.

79 R. A. Corey, *et al.*, Identification and assessment of cardiolipin interactions with *E. coli* inner membrane proteins, *Sci. Adv.*, 2021, **7**, eabh2217.

80 M. Protasoni, *et al.*, Respiratory supercomplexes act as a platform for complex III-mediated maturation of human mitochondrial complexes I and IV, *EMBO J.*, 2020, **39**, e102817.

81 J. A. Letts, K. Fiedorczuk and L. A. Sazanov, The architecture of respiratory supercomplexes, *Nature*, 2016, **537**, 644–648.

82 J. Gu, *et al.*, The architecture of the mammalian respirasome, *Nature*, 2016, **537**, 639–643.

83 M. Wu, J. Gu, R. Guo, Y. Huang and M. Yang, Structure of mammalian respiratory supercomplex $I_1III_2IV_1$, *Cell*, 2016, **167**, 1598–1609.

84 J. S. Sousa, D. J. Mills, J. Vonck and W. Kühlbrandt, Functional asymmetry and electron flow in the bovine respirasome, *eLife*, 2016, **5**, e21290.

85 A. Mühleip, *et al.*, Structural basis of mitochondrial membrane bending by I-II-III_2-IV_2 supercomplex, *bioRxiv*, 2022, DOI: **10.1101/2022.06.26.497646**.